Thermal Damage Detection and Characterization in Porous Materials

H.T. Banks* and Amanda Keck Criner†
Center for Research in Scientific Computation
North Carolina State University
Raleigh, NC 27695-8212

November 30, 2011

Abstract

In this effort we consider damage detection algorithms using thermal probes. The techniques proposed employ models derived from homogenization theory as the model solution in parameter estimation procedures for simulated data for heat flow in a porous medium. We consider data simulated from a model on a perforated domain with isotropic flow and data simulated from a model on a homogeneous domain with anisotropic flow. We report on ordinary least squares methods combined with the method of mappings to detect the presence of damage and to characterize the geometry of the damage.

AMS subject classifications: 93B51, 62B10, 62B15, 62G08, 62H12, 90C31.

Key Words: Damage detection, inverse problems, parameter estimation, perforated domains, homogenization, composite materials, thermal diffusion, ordinary least squares, statistical model comparison.

*Email:htbanks@ncsu.edu
†Email: akcriner@ncsu.edu

Report Documentation Page

Form Approved
OMB No. 0704-0188

1. REPORT DATE	2. REPORT TYPE	3. DATES COVERED
30 NOV 2011		**00-00-2011 to 00-00-2011**

4. TITLE AND SUBTITLE	5a. CONTRACT NUMBER
Thermal Damage Detection and Characterization in Porous Materials	5b. GRANT NUMBER
	5c. PROGRAM ELEMENT NUMBER
6. AUTHOR(S)	5d. PROJECT NUMBER
	5e. TASK NUMBER
	5f. WORK UNIT NUMBER
7. PERFORMING ORGANIZATION NAME(S) AND ADDRESS(ES)	8. PERFORMING ORGANIZATION REPORT NUMBER
North Carolina State University,Center for Research in Scientific Computation,Department of Mathematics,Raleigh,NC,27695-8212	**CRSC-TR11-16**
9. SPONSORING/MONITORING AGENCY NAME(S) AND ADDRESS(ES)	10. SPONSOR/MONITOR'S ACRONYM(S)
	11. SPONSOR/MONITOR'S REPORT NUMBER(S)

12. DISTRIBUTION/AVAILABILITY STATEMENT

Approved for public release; distribution unlimited

13. SUPPLEMENTARY NOTES

14. ABSTRACT

In this effort we consider damage detection algorithms using thermal probes. The techniques proposed employ models derived from homogenization theory as the model solution in parameter estimation procedures for simulated data for heat flow in a porous medium. We consider data simulated from a model on a perforated domain with isotropic flow and data simulated from a model on a homogeneous domain with anisotropic flow. We report on ordinary least squares methods combined with the method of mappings to detect the presence of damage and to characterize the geometry of the damage.

15. SUBJECT TERMS

16. SECURITY CLASSIFICATION OF:			17. LIMITATION OF ABSTRACT	18. NUMBER OF PAGES	19a. NAME OF RESPONSIBLE PERSON
a. REPORT	b. ABSTRACT	c. THIS PAGE			
unclassified	**unclassified**	**unclassified**	**Same as Report (SAR)**	**24**	

1 Introduction

Nondestructive evaluation techniques play an important role in safely using many structures as they age beyond their design lives; these structures include bridges, pipes, and air craft. Though nondestructive evaluation has been studied and used for decades, until recently much of the methodological development has been for homogeneous materials. As composite materials have become more popular, there is a need to develop nondestructive evaluation techniques that accommodate the heterogeneous structure of these materials. A common thermal nondestructive evaluation technique is the flash heat experiment, the use and underlying theory of which has been thoroughly developed for homogeneous materials [11, 15, 25]. The largest order heterogeneity in composite materials is their porosity which is associated with the manufacturing process. In this effort, we include this porosity in simulated thermal data and subsequent analysis of our models. We build on our previous work [3]–[5] which relies heavily on results in [6, 7, 9, 14, 16, 18, 20, 21, 23, 26]. In Section 2 we discuss two models that we use to simulate data; we then consider damage *detection* in Section 3 in the context of statistical model comparison problems, and finally we use ordinary least squares parameter estimation to consider damage *characterization* in Section 4.

2 Mathematical and statistical models

In order to present our method of detecting and characterizing damage, we discuss a few mathematical and statistical models. We developed a method for modeling the flash heat experiment on both damaged and undamaged porous domains in [3] which we use here to simulate data. We model the undamaged domain as a randomly perforated domain Ω. The corresponding undamaged, homogeneous, non perforated domain is denoted by $\hat{\Omega}$ and here is taken as an $L_1 \times L_2$ rectangle $\hat{\Omega} = [0, L_1] \times [0, L_2]$ (we will use $L_1 = 10$ and $L_2 = 2$). We assume n_r randomly placed pores, generated using methods described in [3], which are denoted Ω_i with boundaries $\partial\Omega_i$ for $i = 1, 2 \ldots n_r$. The undamaged perforated domain Ω is given by $\hat{\Omega} \setminus (\cup_{i=1}^{n_r} \Omega_i)$. The four boundaries of $\hat{\Omega}$ which are also the four exterior boundaries of Ω are denoted ω_i for $i = 1, 2, 3, 4$ as depicted in Figure 1. We model the flash heat experiment which approximates an experiment where the bottom boundary $\omega_4 = \{(x, y) | x \in [0, L_1], y = 0\}$ is heated by a flash heat source [25]. Throughout this document, we will refer to ω_4 as the source boundary.

We denote by $\Omega^D(q)$ the damaged porous domain which is constructed using the ellipse

$$E^D(q) = \left\{ (x, y) : \left(\frac{x - x_D}{h_D} \right)^2 + \left(\frac{y - y_D}{v_D} \right)^2 < 1 \right\}$$

with center (x_D, y_D), horizontal semi-axis h_D and vertical semi-axis v_D. The damage (assumed to be in the shape of an elliptical section) and the damaged domain are parameterized by q which specifies (x_D, y_D, h_D, v_D) although throughout this presentation we simplify (without loss of generality) our investigations by considering $y_D = 2.25$ to be fixed. We restrict q so that the center of $E^D(q)$ is above the back boundary ω_2 of $\hat{\Omega}$, and $E^D(q)$ intersects the boundary of $\hat{\Omega}$ at two points on ω_2. The damaged geometry is

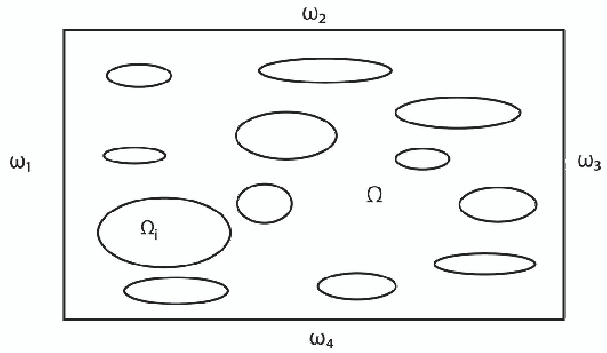

Figure 1: An example randomly perforated domain Ω (enlarged view).

then given by $\Omega^D(q) = (\Omega \cup \mathcal{O}(q)) \setminus E^D(q)$ where $\mathcal{O}(q)$ is the set of ellipses Ω_i in Ω that intersect $E^D(q)$. We denote (with possible reordering) the boundaries of the $n_r^D(q)$ pores remaining in $\Omega^D(q)$ by $\partial\Omega_i$, $i = 1, 2, \ldots n_r^D(q)$. The back boundary, $\omega_2^D(q)$, of $\Omega^D(q)$ is parameterized by (x_D, y_D, h_D, v_D). In order to define $\omega_2^D(q)$ more precisely, we introduce the piecewise defined function

$$r(x;q) = \begin{cases} L_2 & \text{for } 0 \le x \le x_L(q) \\ y_D - v_D\sqrt{1 - \left(\dfrac{x - x_D}{h_D}\right)^2} & \text{for } x_L(q) < x < x_R(q) \\ L_2 & \text{for } x_R(q) \le x \le L_1, \end{cases} \tag{1}$$

where the left end point $x_L(q)$ is given by $x_L(q) = x_D - h_D\sqrt{1 - \left(\dfrac{y_D - L_2}{v_D}\right)^2}$ and the right end point is given by $x_R(q) = x_D + h_D\sqrt{1 - \left(\dfrac{y_D - L_2}{v_D}\right)^2}$. The back boundary of $\Omega^D(q)$ is then given by $\omega_2^D(q) = \{(x, y) : 0 \le x \le L_1 \text{ and } y = r(x;q)\}$.

An example damaged domain is depicted in Figure 2. We model the heat equation on this domain with

$$\begin{cases} \dfrac{\partial}{\partial t}u_D^{\text{rand}} - \alpha\nabla\cdot\left(\nabla u_D^{\text{rand}}\right) = 0 & \text{in } \Omega^D(q)\times(0,T) \\ \alpha\dfrac{\partial}{\partial\eta}u_D^{\text{rand}} = 0 & \text{on } \left(\cup_{i=1}^{n_r^D(q)}\partial\Omega_i\right)\times(0,T) \\ \alpha\dfrac{\partial}{\partial\eta}u_D^{\text{rand}} = 0 & \text{on } \left(\omega_1\cup\omega_2^D(q)\cup\omega_3\right)\times(0,T) \\ \alpha\dfrac{\partial}{\partial\eta}u_D^{\text{rand}} = S_f\mathcal{I}_{[0,t_s]}(t) & \text{on } \omega_4\times(0,T) \\ u^{\text{rand}}(0,\vec{x}) = 0, & \end{cases} \tag{2}$$

with thermal diffusivity $\alpha = 2.9167$, flash heat intensity $S_f = 2.75$, and flash heat duration

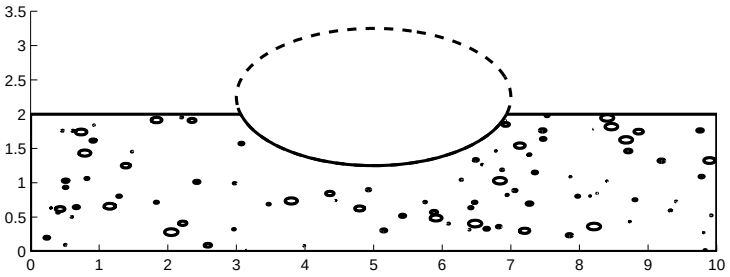

Figure 2: An example geometry $\Omega^D(q)$ for $(x_D, y_D, h_D, v_D) = (5, 2.25, 2, 1)$

$t_s = 0.6$. The heaviside function is given by

$$\mathcal{I}_{[0,t_s]}(t) = \begin{cases} 1, & \text{for } t \in [0, t_s] \\ 0, & \text{otherwise} \end{cases}.$$

We would like to model data that would result from the output of an IR camera. Based on experimental protocols, we assume that each pixel gives the average temperature across a length ℓ on the source boundary ω_4. We denote the corresponding noise free observations by

$$\left(u_D^{\text{rand}}(q)\right)_{ij} = \frac{1}{\ell} \int_{x_i}^{x_i+\ell} u_D^{\text{rand}}(t_j, s, 0; q)\, ds, \tag{3}$$

with pixel length $\ell = 0.57$. To include error associated with the measurement process, we will take data given by realizations of

$$\mathbf{D}_{ij}^{\text{rand}} = \left(u_D^{\text{rand}}(q_0)\right)_{ij} + \sigma_0 \boldsymbol{\beta}_{ij}, \tag{4}$$

where q_0 is the usual "true" parameter value in statistical models [6], the $\boldsymbol{\beta}_{ij}$ are independently identically distributed standard normal random variables. That is $\boldsymbol{\beta}_{ij} \sim \mathcal{N}(0, 1)$ (we use boldface to denote random variables throughout). We will use $\sigma_0 = 0.015$ in all our calculations. It is important to emphasize that $\mathbf{D}_{ij}^{\text{rand}}$ is a random variable with realizations $\mathrm{D}_{ij}^{\text{rand}}$. The realization $\mathrm{D}_{ij}^{\text{rand}}$ would correspond to an observed data set. We take m spatial nodes which correspond to each pixel that begins at $\{x_i\}$ in (3) and n temporal nodes which correspond to the $\{t_j\}$'s in (3).

Based on the encouraging results in [5] which verified that a homogenization approach provides good approximations to solutions u^{rand} for problems on porous domains, we will use a model motivated by homogenization theory as the model solution in our inverse problems. We will also simulate data from this model as in [5] to understand the effect of the error (as compared to data simulated with u_D^{rand}) associated with the approximation derived from homogenization theory on the inverse problem. Methods used in [2, 4, 5, 14, 16, 17, 18, 19, 20, 21, 24] can be used to establish the good approximation of $u_D^{\text{rand}}(t, \vec{x}; q)$ by the homogenization solution $u^D(t, \vec{x}; q)$ where $u^D(t, \vec{x}; q)$ is given by

$$\begin{cases} p_V \dfrac{\partial}{\partial t} u^D - \alpha \nabla \cdot (A^0 \nabla u^D) = 0 & \text{in } \mathcal{T} \times \hat{\Omega}^D(q) \\ \alpha \dfrac{\partial}{\partial \eta_{A^0}} u^D = 0 & \text{on } \mathcal{T} \times \left(\omega_1 \cup \omega_2^D(q) \cup \omega_3\right) \\ \alpha \dfrac{\partial}{\partial \eta_{A^0}} u^D = S_f \mathcal{I}_{[0,t_s]}(t) & \text{on } \mathcal{T} \times \omega_4 \\ u^D(0, \vec{x}) = 0 & \text{for } \vec{x} \in \hat{\Omega}^D, \end{cases} \tag{5}$$

with thermal diffusivity α, proportion of the material in the porous domain p_V (here, $p_V = 0.98$), anisotropy matrix associated with the results of homogenization theory A^0 (see [4] and [5]), intensity of the heat lamp S_f and heaviside function $\mathcal{I}_{[0,t_s]}(t)$. The geometry on which the partial differential equation (5) is defined is given by $\hat{\Omega}^D(q) = \hat{\Omega} \setminus E^D(q)$.

The weak solution of (5) is given by

$$\begin{aligned} p_V \int_{\hat{\Omega}^D(q)} \frac{\partial}{\partial t} u^D(t, \vec{x}; q) \phi(\vec{x}) \, d\vec{x} \quad &+ \quad \alpha \int_{\hat{\Omega}^D(q)} \nabla u^D(t, \vec{x}; q) \cdot A^0 \nabla \phi(\vec{x}) \, d\vec{x} \\ &= \quad S_f \mathcal{I}_{[0,t_s]}(t) \int_{\omega_4} \gamma_{\omega_4}(\phi) \, d\xi_{\omega_4}, \end{aligned} \tag{6}$$

for all test functions $\phi \in H^1(\hat{\Omega}^D)$ where γ_{ω_4} is the trace on ω_4 and ξ_{ω_4} is a parametrization of ω_4. In order to compute a finite element solution of (6), for each iteration of q, a new parameter dependent mesh of $\hat{\Omega}^D(q)$ must be generated. This presents significant computational challenges in carrying out inverse problems. In order to avoid this difficulty, we employ ideas from [10, 11] and transform the homogenized damaged domain $\hat{\Omega}^D(q)$ to a parameter independent reference domain (in this case $\hat{\Omega}$) where we can readily use parameter independent finite elements to carry out the computations. The coordinate transformation is embodied in $\vec{x} = T(q) \circ \vec{z}$ where $T(q)$ is a bijection that maps $\hat{\Omega}$ to $\hat{\Omega}^D(q)$ given by

$$\vec{x} = \begin{bmatrix} x \\ y \end{bmatrix} = T(q)(\vec{z}) = \begin{bmatrix} z_1 \\ \dfrac{r(z_1; q)}{L_2} z_2 \end{bmatrix}. \tag{7}$$

The weak formulation (6) can then be written as (here † is the transpose)

$$p_V \int_{\hat{\Omega}} \frac{\partial}{\partial t} u(t, \vec{z}; q) \phi(\vec{z}) \det\left(\nabla T(\vec{z}; q)\right) d\vec{z} \tag{8}$$

$$- \alpha \int_{\hat{\Omega}} \nabla u(t, \vec{z}; q) \cdot \nabla T(\vec{z}; q)^{-1} A^0 \left(\nabla T(\vec{z}; q)^\dagger\right)^{-1} \nabla \phi(\vec{z}) \det(\nabla T(\vec{z}; q)) \, d\vec{z}$$

$$= S_f \mathcal{I}_{[0,t_s]}(t) \int_{\omega_4} \gamma_{\omega_4}(\phi) \, d\xi_{\omega_4}, \text{ for all } \phi \in H^1(\hat{\Omega}),$$

by making the coordinate transformation $\vec{x} = T(\vec{z}; q)$ with u on $\hat{\Omega}$ defined by $u(t, \vec{z}; q) = u^D(t, T(\vec{z}; q); q)$. Noting that

$$\nabla T(\vec{z}; q) = \begin{bmatrix} 1 & 0 \\ \dfrac{r'(z_1; q)}{L_2} z_2 & \dfrac{r(z_1; q)}{L_2} \end{bmatrix}, \tag{9}$$

and $\det(\nabla T(\vec{z}; q)) = \dfrac{r(z_1; q)}{L_2}$, we may rewrite (8) as

$$\begin{aligned} \frac{p_V}{L_2} \int_{\hat{\Omega}} \frac{\partial}{\partial t} u(t, \vec{z}; q) \phi(\vec{z}) r(z_1; q)\, d\vec{z} \;\; &- \;\; \alpha \int_{\hat{\Omega}} \nabla u(t, \vec{z}; q) \cdot B(\vec{z}; q) \nabla \phi(\vec{z})\, d\vec{z} \\ &= \;\; S_f \mathcal{I}_{[0,t_s]}(t) \int_{\omega_4} \gamma_{\omega_4}(\phi)\, d\xi_{\omega_4}. \end{aligned} \tag{10}$$

In (10), $B(\vec{z}; q)$ is a 2×2 matrix with entries

$$\begin{aligned} b_{11}(\vec{z}; q) &= a^0_{11} \frac{r(z_1; q)}{L_2} \\ b_{12}(\vec{z}; q) &= -a^0_{11}\, z_2\, \frac{r'(z_1; q)}{L_2} + a^0_{12} \\ b_{21}(\vec{z}; q) &= -a^0_{11}\, z_2\, \frac{r'(z_1; q)}{L_2} + a^0_{21} \\ b_{22}(\vec{z}; q) &= a^0_{11}\, (z_2)^2 \frac{(r'(z_1; q))^2}{r(z_1; q) L_2} - \frac{r'(z_1; q)}{r(z_1; q)} z_2 (a^0_{12} + a^0_{21}) + a^0_{22} \frac{L_2}{r(z_1; q)}, \end{aligned} \tag{11}$$

where a^0_{ij} are the entries of A^0. Using the finite element approximation $\tilde{u}^N(t, \vec{z}; q) = \sum_{j=1}^{N} u^N_j(t; q) \phi^N_j(\vec{z})$ where the $\phi^N_j(\vec{z})$ are piecewise affine two dimensional basis elements (e.g., see [12]), we may solve for the time dependent coefficients $\vec{u}^N = (u^N_1, \ldots, u^N_N)^\dagger$ by solving the ordinary differential equation

$$p_V C^N(q) \frac{d}{dt} \vec{u}^N(t) + \alpha K^N(q) \vec{u}^N(t) = S_f \mathcal{I}_{[0,t_s]}(t) \vec{f}^N, \tag{12}$$

where

$$\begin{aligned} C^N_{ij}(q) &= \frac{1}{L_2} \int_{\hat{\Omega}} \phi^N_j(\vec{z}) \phi^N_i(\vec{z}) r(z_1; q)\, d\vec{z} \qquad \text{for } i, j = 1, 2, \ldots N \\ K^N_{ij}(q) &= \int_{\hat{\Omega}} \nabla \phi^N_j(\vec{z}) \cdot B(\vec{z}; q) \nabla \phi^N_i(\vec{z})\, d\vec{z} \quad \text{for } i, j = 1, 2, \ldots N \\ \vec{f}^N_i &= \int_{\omega_4} \gamma_{\omega_4}(\phi^N_i)\, d\xi_{\omega_4} \qquad \text{for } i = 1, 2, \ldots N. \end{aligned} \tag{13}$$

As in formulating $(u^{\text{rand}}_D(q))_{ij}$ in (3), we use the average of the solution over intervals of length $\ell = 0.57$ (which represents the pixel length) in our model solution. We will use

model solutions given by (recall $z_1 = x$)

$$U_{ij}^N(q) = \frac{1}{\ell}\int_{x_i}^{x_i+\ell} \tilde{u}^N(t_j, x, 0; q)\, dx \tag{14}$$

where $\tilde{u}^N(t, \vec{z}; q)$ is the finite element solution obtained using (12).

We will use $U_{ij}^N(q)$ as defined in (14) as a model solution in our data analysis. To consider the effect of model discrepancy on our statistical procedures, as in [5], we also consider (in addition to the data generated using (4)) data generated using the finite element solution given through (12). Specifically, we will consider data generated using

$$\mathbf{D}_{ij} = \mathbf{D}_{ij}^N = U_{ij}^N(q_0) + \sigma_0 \boldsymbol{\beta}_{ij}, \tag{15}$$

where as in (4), $\boldsymbol{\beta}_{ij} \sim \mathcal{N}(0, 1)$. The realizations of the random variables $\mathbf{D}_{ij}$ are denoted D_{ij}. We remark that we will suppress the index N since it will be fixed throughout. Computational studies of choosing appropriate values of N in (12) and of N^D in corresponding finite element solutions of u_D^{rand} in (2) were carried out before beginning our inverse problem calculations. Values for N ranging between 48 and 2337 and for N^D ranging between 64 and 3193 were tested. Above $N = 609$ and $N^D = 829$ there was little change in computed solutions although computational times increased substantially for larger values than these. Therefore we chose these values for the computational results for detection and characterization reported on here.

We will consider two types of statistically-based procedures. We will formulate a comparison technique to detect damage using a model comparison test which is developed in [8] and illustrated in [6, 12]. We will then demonstrate use of ordinary least squares parameter estimation to estimate the parameters (x_D, h_D, v_D) which characterize the damage.

3 Damage Detection

Both the damage detection methodology and the ordinary least squares (OLS) parameter estimation involve minimizing the OLS cost functional which is given by

$$J(q) = \sum_{i=1}^{m}\sum_{j=1}^{n} (U_{ij}(q) - \mathrm{data}_{ij})^2. \tag{16}$$

(As noted above, since N is assumed fixed throughout, we will suppress the corresponding superscripts on variables such as $U_{ij}^N(q)$ and numerous others throughout the remainder of this presentation.) The term data_{ij} represents without loss of generality either of the realizations D_{ij} or $\mathrm{D}_{ij}^{\text{rand}}$. Here we emphasize that the function $J(q)$ of the realization data_{ij} is a realization of a function of a random variable $\mathbf{data}_{ij}$ given by

$$\mathbf{J}(q) = \sum_{i=1}^{m}\sum_{j=1}^{n} (U_{ij}(q) - \mathbf{data}_{ij})^2. \tag{17}$$

where $\mathbf{data}_{ij}$ represents either the finite element based random process $\mathbf{D}_{ij}$ or the random porous domain random process $\mathbf{D}_{ij}^{\text{rand}}$.

Damage detection may be considered using a hypothesis or model comparison test. The case where there is no damage can be modeled with an ellipse $E^D(q)$ that has a horizontal semi-axis length of zero. So when $h_D = 0$, we have that there is no damage in the sample. We use this to formulate a hypothesis test. The null hypothesis (there is no damage) is given by $H_0 : h_D = 0$, and the alternative hypothesis (there is possible damage) is given by $H_A : h_D \neq 0$. We will define the set of parameters corresponding to the null hypothesis by $\mathcal{Q}_H = \{q = (x_D, h_D, v_D, \alpha) | h_D = 0, q \in \mathcal{Q}\}$. The full admissible parameter set $\mathcal{Q} = \{q = (x_D, h_D, v_D, \alpha) \in \mathbb{R}^4\}$ is assumed to be a bounded subset of the nonnegative quadrant of $\mathbb{R}^4$. Using methods described in [6, 8, 12], we consider two parameter estimates

$$\hat{q}_H = \arg \min_{q \in \mathcal{Q}_H} J(q), \tag{18}$$

and

$$\tilde{q} = \arg \min_{q \in \mathcal{Q}} J(q), \tag{19}$$

where the parameter estimates are realizations of random variables. The corresponding two estimators are given by

$$\hat{\mathbf{q}}_{\mathbf{H}} = \arg \min_{q \in \mathcal{Q}_H} \mathbf{J}(q), \tag{20}$$

and

$$\tilde{\mathbf{q}} = \arg \min_{q \in \mathcal{Q}} \mathbf{J}(q), \tag{21}$$

respectively. The estimates are, of course, realizations of the random estimators.

This model comparison methodology uses the test statistic $\boldsymbol{X}$ given by

$$\boldsymbol{X} = nm \left(\frac{\boldsymbol{J}(\hat{\boldsymbol{q}}_{\boldsymbol{H}}) - \boldsymbol{J}(\tilde{\boldsymbol{q}})}{\boldsymbol{J}(\tilde{\boldsymbol{q}})} \right) \tag{22}$$

where nm is the total number of observations (there are n temporal nodes and m spatial nodes). The random variable $\boldsymbol{X}$ then has realizations X which are given by

$$X = nm \left(\frac{J(\hat{q}_H) - J(\tilde{q})}{J(\tilde{q})} \right), \tag{23}$$

where $\hat{q}_H$ is the corresponding realization of $\hat{\boldsymbol{q}}_{\boldsymbol{H}}$ and $\tilde{q}$ is the corresponding realization of $\tilde{\boldsymbol{q}}$.

The results of [8] indicate that if H_0 is true then the random variable $\boldsymbol{X}$ approaches in distribution (as sample size nm increases) a random variable which follows a chi-square distribution with one degree of freedom (denoted $\chi^2(1)$). This can be used in the following way. If we would like to reject our null hypothesis with 95% confidence, we would calculate the corresponding significance level $\bar{\alpha} = 0.05$ (note that confidence $= (1 - \bar{\alpha}) \times 100\%$) and the corresponding threshold value τ defined by the probability $P(\boldsymbol{X} > \tau) = \bar{\alpha}$. Using a $\chi^2(1)$ cumulative distribution function table, for $\bar{\alpha} = 0.05$, we find $\tau = 3.84$. Then for any realization X with $X > 3.84$, we may reject with at least 95% confidence. The minimum

Pixel Set	x_i values
Left 11 Nodes	$x_i = \ell(i-1)$ for $i \in \{1, 2, \dots 11\}$
Right 11 Nodes	$x_i = \ell(i-1) + 6\ell$ for $i \in \{1, 2, \dots 11\}$
Evenly Spaced 11 Nodes	$x_i \in \{0, 2\ell, 5\ell, 6\ell, 7\ell, 9\ell, 10\ell, 12\ell, 13\ell, 15\ell, 16\ell\}$
All 17 Nodes	$x_i = \ell(i-1)$, for $i \in \{1, 2, 3 \dots, 17\}$

Table 1: Pixel sets used throughout the computations with $\ell = 0.57$

value α^* at which the null hypothesis can be rejected for a realization X is called the p-value, that is

$$\text{p-value} = \alpha^* = \min P(\boldsymbol{X} > X).$$

Thus, the closer a p-value is to zero, the more confidence with which one may reject the null hypothesis (for further discussion see [6, 8, 12]).

We considered simulations using four different sets of spatial nodes (corresponding to pixels) which are listed in Table 1. We used these values to generate the data D_{ij} and $\mathrm{D}_{ij}^{\mathrm{rand}}$. We considered eighteen different damages. In each example we assumed $y_D = 2.25$ is known. We considered one series of nine damages of increasing size with center $x_D = 3$ and another series of nine damages increasing size with center $x_D = 5$. For these examples, we used $v_D^i = 0.3 + 0.05(i-1)$ and $h_D^i = 2v_D^i$ for $i \in \{1, 2, 3 \dots 9\}$. Example damages for $x_D = 3$ and $i = 1, 2, 8$, and 9 are depicted in Figures 3 (a), (b), (c) and (d), respectively. In Figures 4-7, we depict for comparison the results of this damage detection technique for data sets simulated with (4) and (15) using spatial nodes given in Table 1 and temporal nodes given by $t_j = 0.6 + \dfrac{1}{120} j$ for $j \in \{1, 2, \dots 92\}$.

The threshold value of the statistic τ at which one may reject the null hypothesis with 99.9% confidence is $\tau = 10.8$. Thus, if $X > 10.8$ one may reject the null hypothesis with 99.9% confidence. The larger X, the more confidence there is in rejecting the null hypothesis.

In Figures 4–7 (a) we depict the test statistic X using (23) for $x_D = 3$, and in Figures 4–7 (b) we depict the test statistic X using (23) for $x_D = 5$, in Figures 4–7 (c) we depict the p-value for $x_D = 3$, and in Figures 4–7 (d) we depict the p-value for $x_D = 5$. We observe that for the damages above 3% the test statistics X become very large. There is no clear difference between the values of the test statistic X when calculated using D_{ij} than when using $\mathrm{D}_{ij}^{\mathrm{rand}}$ which suggests that the model discrepancy associated with the difference between u_D^{rand} (the solution of (2)) and u^D, the solution of (5), or its approximation given by (12), does not substantially affect this test statistic.

Using the left most nodes (see Table 1) in Figures 4 (c)–(d), Figures 5 (c) and (d), we depict the p-values for $x_D = 3$ and $x_D = 5$, respectively. For both of these series of damages, the p-values calculated using $\mathrm{D}_{ij}^{\mathrm{rand}}$ are very low suggesting that one may reject the null hypothesis with high confidence. The p-values calculated using D_{ij} are larger, though still sufficiently small to reject the null hypothesis with 90% confidence. In every example, for damages which occupied more than 3% of the area, the p-values were close to zero which corresponds to high confidence in rejecting the null hypothesis that there is no damage. The only situations in which the p-values were larger were for

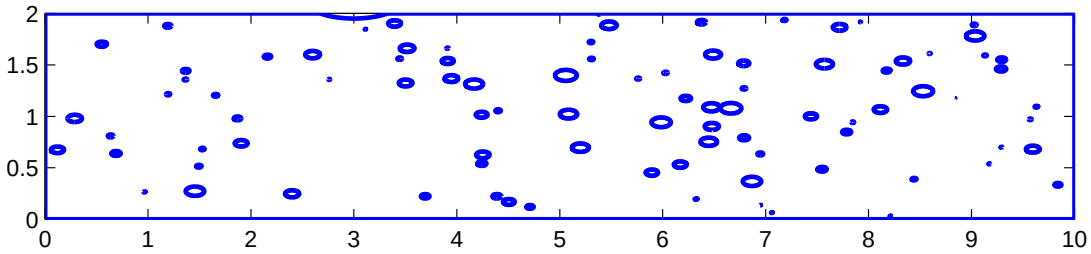

(a) Randomly perforated damaged geometry for $(x_D, h_D, v_D) = (3, 0.6, 0.3)$

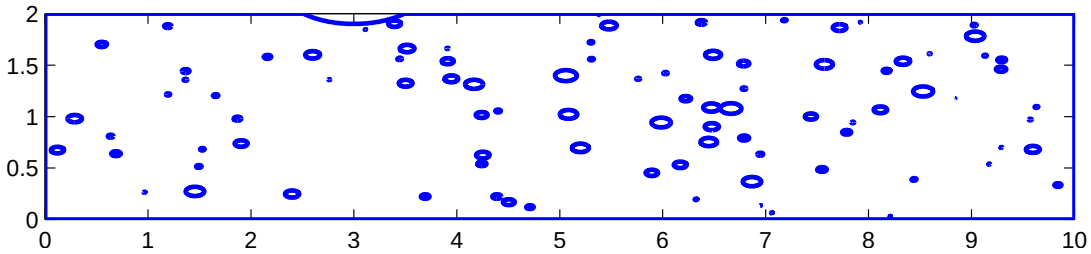

(b) Randomly perforated damaged geometry for $(x_D, h_D, v_D) = (3, 0.7, 0.35)$

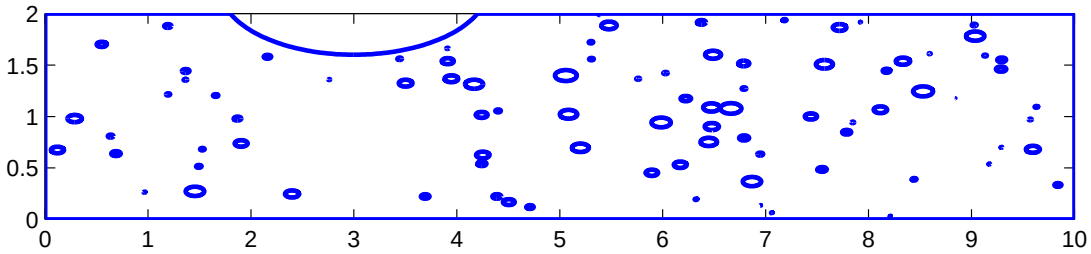

(c) Randomly perforated damaged geometry for $(x_D, h_D, v_D) = (3, 1.3, 0.65)$

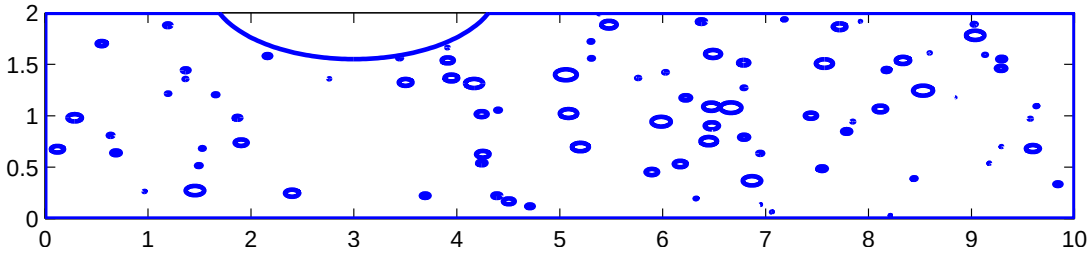

(d) Randomly perforated damaged geometry for $(x_D, h_D, v_D) = (3, 1.4, 0.7)$

Figure 3: The example perforated damaged geometry for (a) $(x_D, h_D, v_D) = (3, 0.6, 0.3)$, (b) for $(x_D, h_D, v_D) = (3, 0.7, 0.35)$, (c) for $(x_D, h_D, v_D) = (3, 1.3, 0.65)$, (d) for $(x_D, h_D, v_D) = (3, 1.4, 0.7)$, respectively.

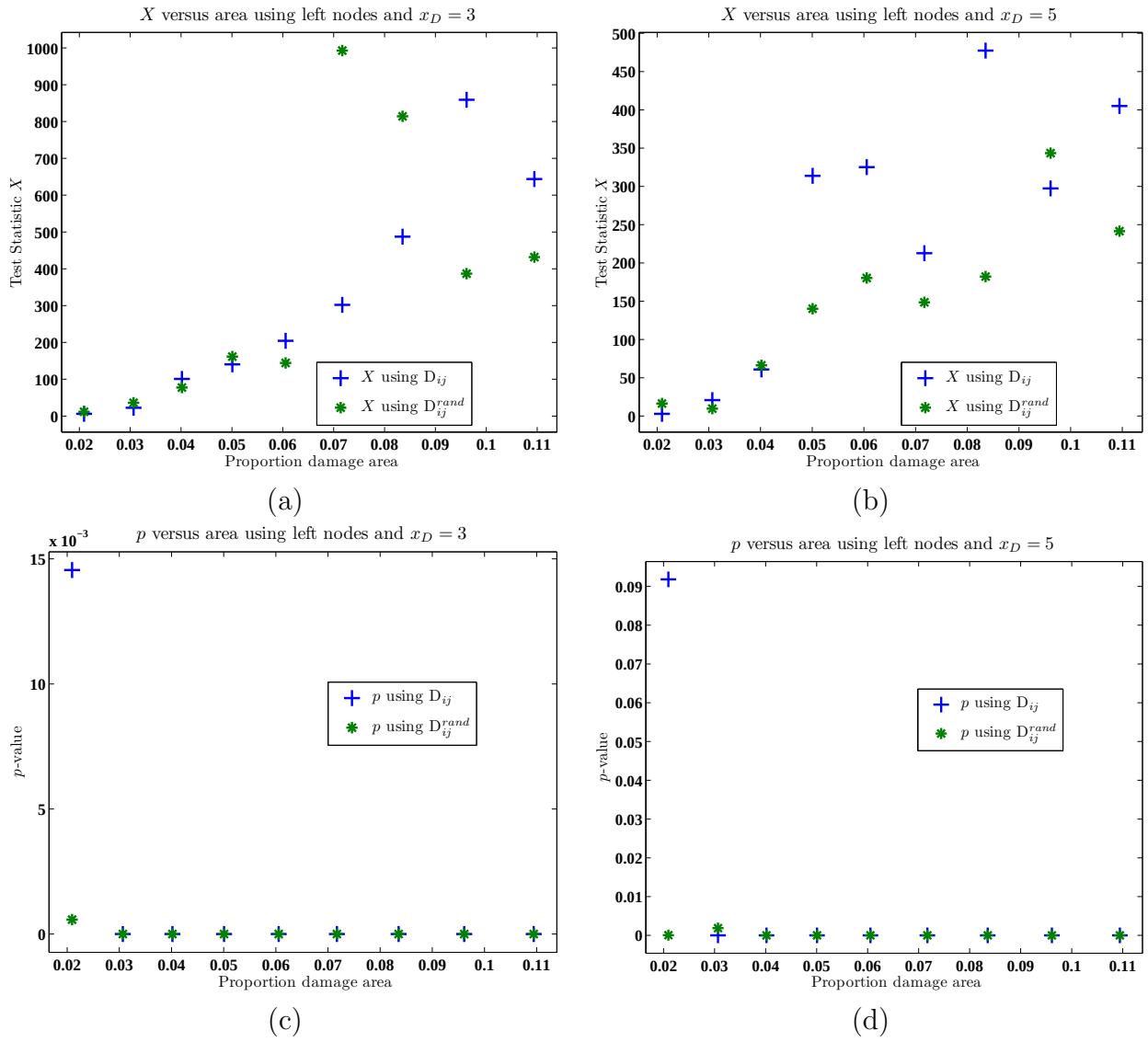

Figure 4: Results using the left nodes for observations: Test statistic X versus proportion of area occupied by damage for (a) $x_D = 3$, (b) for $x_D = 5$; (c) the corresponding p-values versus proportion of area occupied by damage for $x_D = 3$, and (d) for $x_D = 5$.

$(h_D, v_D) = (0.6, 0.3)$ and $(h_D, v_D) = (0.7, 0.35)$ so we will focus on these examples in the remainder of this section.

The results of damage detection using the right set of nodes (see Table 1) are depicted in Figures 5(a)–(d). We see similar results for these pixels as for the left subset of pixels. In the example where $x_D = 3$, both $(h_D, v_D) = (0.6, 0.3)$ and $(h_D, v_D) = (0.7, 0.35)$ have high p-values when calculated using D_{ij} so that the null hypothesis cannot be rejected with even 50% confidence in Figure 5(c). Using right pixels with data generated with $x_D = 5$, the p-values using D_{ij} are low for both $(h_D, v_D) = (0.6, 0.3)$ and $(h_D, v_D) = (0.7, 0.35)$ with rejection of the null hypothesis with 90% confidence as depicted in Figure 5 (d). The result of this test using $\mathrm{D}_{ij}^{\mathrm{rand}}$ gives a low p-value for the example damage with $(x_D, h_D, v_D) = (5, 0.6, 0.3)$, as we observe in Figure 5(d), but for $(5, 0.7, 0.35)$ the p-value is over 0.25 and we may only reject the null hypothesis with 70%.

We turn to the data from evenly spaced nodes in Figures 6 (c) and (d), where the p-values are very low for damage over 3%. For the smaller damages with $(h_D, v_D) = (0.6, 0.3)$ and $(h_D, v_D) = (0.7, 0.35)$, the p-values calculated using D_{ij} are high so that one cannot reject the null hypothesis with very high confidence as can be seen in Figures 6 (c) and (d). The p-values using $\mathrm{D}_{ij}^{\mathrm{rand}}$ are only large for the smallest damage in Figure 6 (c) and (d). For this example one may reject the null hypothesis with 95% confidence for $x_D = 3$ in Figure 6(c) and 85% confidence for $x_D = 5$ in Figure 6(d).

Finally, in Figures 7 (a)–(d) we depict the results obtained by using the entire set of spatial nodes (all seventeen pixels). All examples, except the smallest example damages $(h_D, v_D) = (0.6, 0.3)$ for both $x_D = 3$ and $x_D = 5$, have very small p-values which indicates that the null hypothesis using all spatial nodes can be rejected for damages over 3%.

In summary, our simulations suggest that for the damages investigated here, the methods we propose for damage detection appear useful with porous materials.

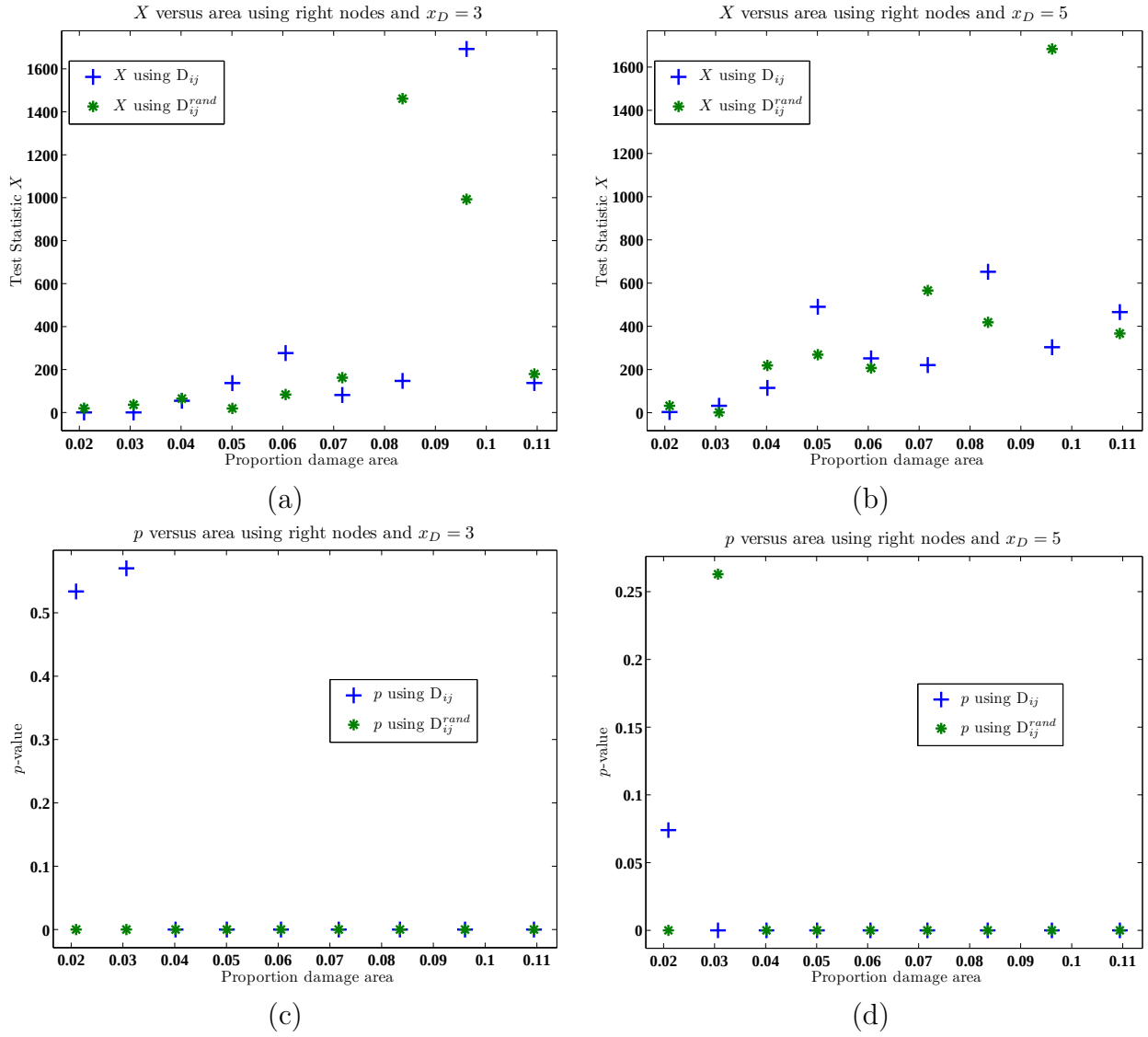

Figure 5: Results using the right nodes for observations: Test statistic X versus proportion of area occupied by damage for (a) $x_D = 3$, (b) for $x_D = 5$; (c) the corresponding p-values versus proportion of area occupied by damage for $x_D = 3$, and (d) for $x_D = 5$.

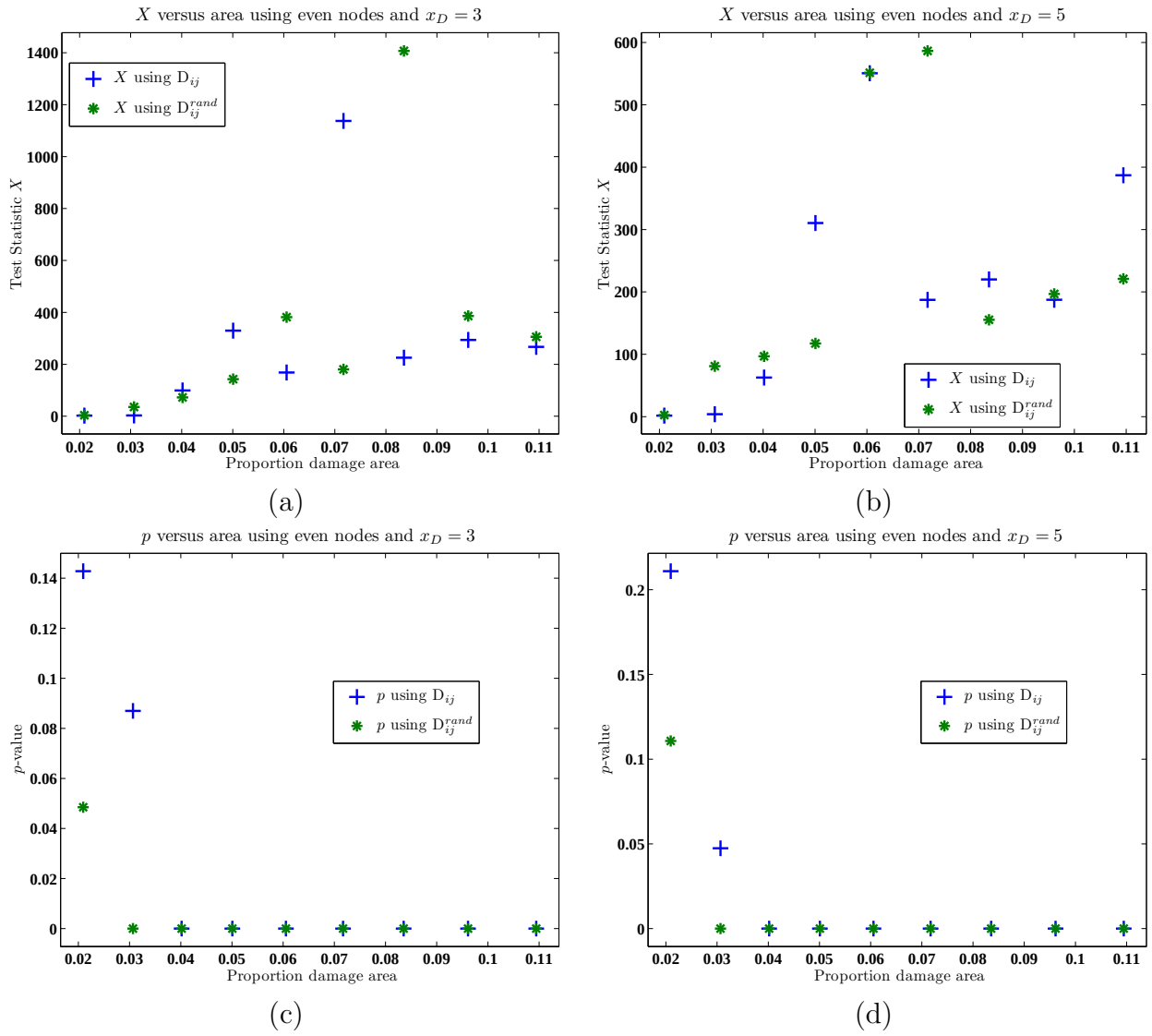

Figure 6: Results using the evenly spaced nodes for observations: Test statistic X versus proportion of area occupied by damage for (a) $x_D = 3$, (b) for $x_D = 5$; (c) the corresponding p-values versus proportion of area occupied by damage for $x_D = 3$, and (d) for $x_D = 5$.

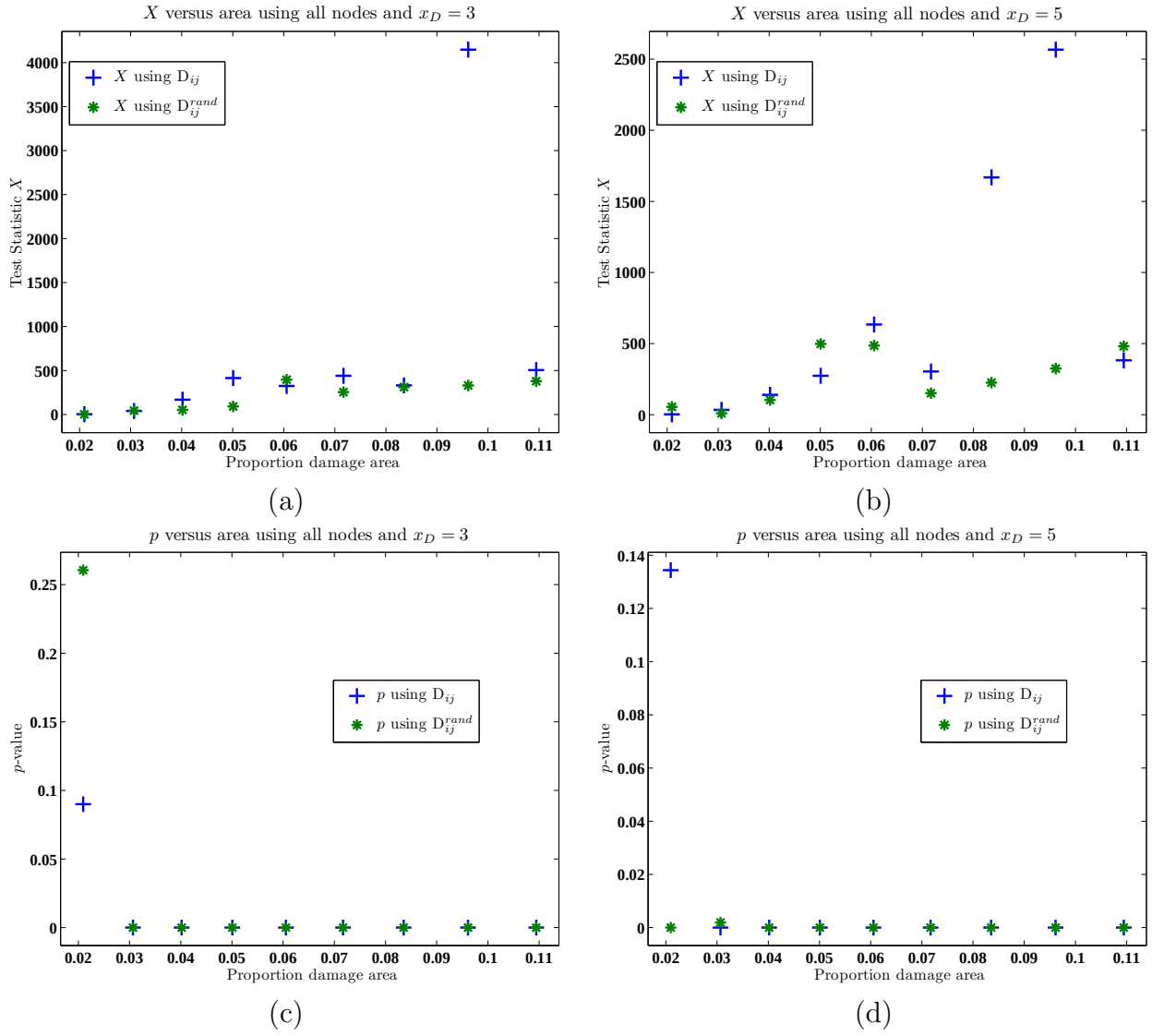

Figure 7: Results using all of the nodes for observations: Test statistic X versus proportion of area occupied by damage for (a) $x_D = 3$, (b) for $x_D = 5$; (c) the corresponding p-values versus proportion of area occupied by damage for $x_D = 3$, and (d) for $x_D = 5$.

4 Damage Characterization

Though the detection techniques that we discussed in Section 3 can be used to detect damage, we would also like to characterize the extent of damage once its presence is suspected. We will consider the ordinary least squares (OLS) estimation procedure in order to characterize parameterized damages. Under certain conditions, this procedure can provide standard error estimates for the damage related parameter estimates. The OLS parameter estimate given by

$$\hat{q} = \arg\min_{q \in \mathcal{Q}} J(q), \tag{24}$$

where now we consider the parameter set $q = (x_D, h_D, v_D)$ and J is given by (16). The OLS error variance estimate is given by

$$\hat{\sigma}^2 = \frac{J(\hat{q})}{nm - p} \tag{25}$$

where p is the number of parameters defining the dimension of the admissible parameter set $\mathcal{Q}$, n is the number of temporal nodes and m is the number of spatial nodes (pixels).

The covariance matrix estimate [6, 13, 23] is then given by

$$\Sigma(\hat{q}) = \hat{\sigma}^2 \left(\chi^\dagger(\hat{q})\chi(\hat{q})\right)^{-1}, \tag{26}$$

where $\chi(\hat{q})$ is the matrix of sensitivities with entries

$$\chi_{i+m(j-1),k}(q) = \left.\frac{\partial}{\partial q_k} U_{ij}(\zeta)\right|_{\zeta=q}, \tag{27}$$

for $i = 1, 2, \ldots, m$, $j = 1, 2, \ldots, n$, and $k = 1, 2, \ldots p$. The details of the calculations of these sensitivities using associated sensitivity partial differential equations are tedious but straight forward and will not be given here; the interested reader may find them given in Appendix A.2 of [22]. The asymptotic standard error estimate for the kth parameter is then given by

$$\mathrm{SE}(\hat{q}) \approx \sqrt{\Sigma_{kk}(\hat{q})}. \tag{28}$$

We will use a very large number of nodes so for all our parameter sets, the 95% confidence interval [6, 13] is given by

$$95\%\text{Confidence Interval } = (\hat{q} - 1.96\,\mathrm{SE}(\hat{q}), \hat{q} + 1.96\,\mathrm{SE}(\hat{q}))$$

and the 99% confidence interval is given by

$$99\%\text{Confidence Interval } = (\hat{q} - 2.58\,\mathrm{SE}(\hat{q}), \hat{q} + 2.58\,\mathrm{SE}(\hat{q})).$$

Unlike the situation for damage detection, there are significant differences in the results using realizations of $\mathbf{D}_{ij}$ versus realizations of $\mathbf{D}_{ij}^{\mathrm{rand}}$. All three variables (x_D, h_D, v_D) appear to be well estimated using the realizations of $\mathbf{D}_{ij}$. However, there are many cases where using realizations of $\mathbf{D}_{ij}^{\mathrm{rand}}$ yield values that are significantly different than the true

Table 2: The estimated geometries for $(x_D, h_D, v_D) = (3, 1, 0.5)$

Nodes	$n \times m$	Data	$\hat{\sigma}^2$	$(\hat{x}_D, \hat{h}_D, \hat{v}_D)$	(SE($\hat{x}_D$),SE($\hat{h}_D$),SE($\hat{v}_D$))
Left	1012	$\mathbf{D}$	0.028	(2.9, 0.941, 0.51)	(0.086, 0.25, 0.071)
		$\mathbf{D}^{\text{rand}}$	0.03	(3.84, 0.653, 0.59)	(0.073, 0.18, 0.099)
Right	1012	$\mathbf{D}$	0.027	(3.01, 1.01, 0.49)	(1.1, 1.4, 0.45)
		$\mathbf{D}^{\text{rand}}$	0.031	(4.09, 0.626, 0.58)	(0.084, 0.2, 0.12)
Even	1012	$\mathbf{D}$	0.028	(2.95, 0.948, 0.5)	(0.13, 0.41, 0.1)
		$\mathbf{D}^{\text{rand}}$	0.031	(3.88, 0.564, 0.64)	(0.083, 0.15, 0.12)
All	1564	$\mathbf{D}$	0.024	(2.93, 0.934, 0.51)	(0.08, 0.26, 0.07)
		$\mathbf{D}^{\text{rand}}$	0.027	(3.89, 0.596, 0.62)	(0.067, 0.14, 0.1)

Table 3: The estimated geometries for $(x_D, h_D, v_D) = (3, 2, 1)$

Nodes	$n \times m$	Data	$\hat{\sigma}^2$	$(\hat{x}_D, \hat{h}_D, \hat{v}_D)$	(SE($\hat{x}_D$),SE($\hat{h}_D$),SE($\hat{v}_D$))
Left	1012	$\mathbf{D}$	0.032	(3.01, 1.99, 1)	(0.023, 0.059, 0.015)
		$\mathbf{D}^{\text{rand}}$	0.048	(3.02, 3.02, 0.76)	(0.041, 0.1, 0.012)
Right	1012	$\mathbf{D}$	0.03	(3.02, 2.01, 1)	(0.29, 0.41, 0.044)
		$\mathbf{D}^{\text{rand}}$	0.045	(3.6, 1.71, 0.93)	(0.27, 0.48, 0.072)
Even	1012	$\mathbf{D}$	0.03	(3.01, 1.99, 1)	(0.027, 0.068, 0.018)
		$\mathbf{D}^{\text{rand}}$	0.052	(3.02, 2.87, 0.78)	(0.044, 0.11, 0.017)
All	1564	$\mathbf{D}$	0.026	(3.01, 1.98, 1)	(0.021, 0.054, 0.015)
		$\mathbf{D}^{\text{rand}}$	0.06	(3.01, 1.94, 0.95)	(0.037, 0.1, 0.027)

values. In some of these cases, the standard errors are sufficiently large so that a 99% confidence interval covers these values.

In Table 2, which presents the results using $(x_D, h_D, v_D) = (3, 1, 0.5)$, the estimate $(\hat{x}_D, \hat{h}_D, \hat{v}_D)$ for the data D_{ij} is much closer to the "true" value than that for the data $\mathrm{D}_{ij}^{\text{rand}}$. For this example using a realization of $\mathbf{D}_{ij}^{\text{rand}}$, for each set of pixels, the values $(\hat{h}_D, \hat{v}_D)$ are within the 95% confidence intervals though the estimated values are not close to the "true" value. The estimates of $\hat{x}_D$ for each set of pixels are not only far from the value $x_D = 3$ but the standard error SE($\hat{x}_D$) is sufficiently small so that for each pixel set the 99% confidence interval does not contain the value $x_D = 3$.

We also considered the realizations D_{ij} and $\mathrm{D}_{ij}^{\text{rand}}$ for $(x_D, h_D, v_D) = (3, 2, 1)$ (see Table 3). Again, for the results obtained by using the realization D_{ij}, the corresponding parameter estimates are close to their "true" values and the standard errors are reasonable for all pixel sets. The corresponding realizations of $\mathbf{D}_{ij}^{\text{rand}}$ with all pixel sets, except the right pixel set, yield estimates $\hat{x}_D$ that are very close to the value $x_D = 3$. For every set of pixels, the value $x_D = 3$ is covered by the 95% confidence interval. The right pixel set and the full pixel set ("All 17 Nodes" in Table 1) have values of $\hat{h}_D$ close to $h_D = 2$

Table 4: The estimated geometries for $(x_D, h_D, v_D) = (5, 1, 0.5)$

Nodes	$n \times m$	Data	$\hat{\sigma}^2$	$(\hat{x}_D, \hat{h}_D, \hat{v}_D)$	(SE($\hat{x}_D$),SE($\hat{h}_D$),SE($\hat{v}_D$))
Left	1012	$\mathbf{D}$	0.028	(5.08, 1.04, 0.49)	(0.1, 0.47, 0.086)
		$\mathbf{D}^{\text{rand}}$	0.032	(5.87, 1.12, 0.51)	(0.19, 0.65, 0.11)
Right	1012	$\mathbf{D}$	0.027	(4.92, 0.944, 0.51)	(0.088, 0.26, 0.071)
		$\mathbf{D}^{\text{rand}}$	0.031	(5.4, 1.08, 0.51)	(0.089, 0.28, 0.067)
Even	1012	$\mathbf{D}$	0.028	(4.95, 0.934, 0.52)	(0.12, 0.37, 0.094)
		$\mathbf{D}^{\text{rand}}$	0.033	(5.5, 1.12, 0.51)	(0.11, 0.3, 0.073)
All	1564	$\mathbf{D}$	0.024	(5.05, 1.07, 0.48)	(0.092, 0.4, 0.072)
		$\mathbf{D}^{\text{rand}}$	0.028	(5.64, 1.39, 0.45)	(0.12, 0.41, 0.052)

Table 5: The estimated geometries for $(x_D, h_D, v_D) = (5, 2, 1)$

Nodes	$n \times m$	Data	$\hat{\sigma}^2$	$(\hat{x}_D, \hat{h}_D, \hat{v}_D)$	(SE($\hat{x}_D$),SE($\hat{h}_D$),SE($\hat{v}_D$))
Left	1012	$\mathbf{D}$	0.03	(4.99, 2.01, 1)	(0.037, 0.098, 0.02)
		$\mathbf{D}^{\text{rand}}$	0.038	(4.96, 1.99, 0.92)	(0.044, 0.12, 0.025)
Right	1012	$\mathbf{D}$	0.029	(5, 2, 1)	(0.027, 0.078, 0.018)
		$\mathbf{D}^{\text{rand}}$	0.035	(5.17, 2.31, 0.86)	(0.04, 0.1, 0.017)
Even	1012	$\mathbf{D}$	0.03	(5, 2.02, 1)	(0.027, 0.066, 0.017)
		$\mathbf{D}^{\text{rand}}$	0.041	(5.12, 2.22, 0.87)	(0.04, 0.1, 0.02)
All	1564	$\mathbf{D}$	0.026	(4.99, 2.01, 1)	(0.022, 0.058, 0.015)
		$\mathbf{D}^{\text{rand}}$	0.038	(5.1, 2.14, 0.89)	(0.031, 0.083, 0.017)

which is covered by their respective 95% confidence intervals. The estimates $\hat{h}_D$ for the left and evenly spaced pixel set are both over estimates and are far from the value $h_D = 2$ when this distance is compared to the estimated standard errors. Neither the left nor evenly spaced subset of pixels provided estimates in which $h_D = 2$ is covered by the 95% confidence interval. We see that the estimates $\hat{v}_D$ in this case are close to the value $v_D = 1$ for the full and right pixel sets while the estimates $\hat{v}_D$ are much smaller than $v_D = 1$ for the left and evenly spaced pixel sets.

The results of the OLS parameter estimation procedure for realizations of $\mathbf{D}_{ij}^{\text{rand}}$ with $(x_D, h_D, v_D) = (5, 1, 0.5)$ in Table 4 are similar to the results in Table 2 with $(x_D, h_D, v_D) = (3, 1, 0.5)$. The estimates of $(\hat{h}_D, \hat{v}_D)$ are close to $(h_D, v_D) = (1, 0.5)$ and the standard errors $(\text{SE}(\hat{h}_D), \text{SE}(\hat{v}_D))$ are sufficiently large that $(h_D, v_D) = (1, 0.5)$ is within two standard errors of the parameter estimate $(\hat{h}_D, \hat{v}_D)$ for all sets of pixels that we considered. The estimate $\hat{x}_D$ for the realization $\text{D}_{ij}^{\text{rand}}$ is much larger than $x_D = 5$ (though this effect is not as severe as for $x_D = 3$ in Table 2) and the standard errors are small so that for each set of pixels the value $x_D = 5$ is not covered by the resepective 95% confidence interval.

Using the realization $\text{D}_{ij}^{\text{rand}}$ in Table 5 with damage given by $(x_D, h_D, v_D) = (5, 2, 1)$ for

Table 6: The estimated geometries for $(x_D, h_D, v_D) = (3, 0.5, 1)$

Nodes	$n \times m$	Data	$\hat{\sigma}^2$	$(\hat{x}_D, \hat{h}_D, \hat{v}_D)$	(SE($\hat{x}_D$),SE($\hat{h}_D$),SE($\hat{v}_D$))
Left	1012	$\mathbf{D}$	0.028	$(3.05, 0.512, 0.97)$	$(0.037, 0.015, 0.047)$
		$\mathbf{D}^{\text{rand}}$	0.03	$(3.39, 0.987, 0.66)$	$(0.062, 0.16, 0.063)$
Right	1012	$\mathbf{D}$	0.028	$(2.88, 0.389, 1.2)$	$(0.066, 0.087, 0.51)$
		$\mathbf{D}^{\text{rand}}$	0.032	$(2.96, 0.476, 1.1)$	$(0.12, 0.032, 0.38)$
Even	1012	$\mathbf{D}$	0.028	$(2.99, 0.513, 0.97)$	$(0.047, 0.018, 0.068)$
		$\mathbf{D}^{\text{rand}}$	0.031	$(3.35, 0.962, 0.67)$	$(0.082, 0.22, 0.084)$
All	1564	$\mathbf{D}$	0.025	$(3.05, 0.492, 1)$	$(0.031, 0.014, 0.039)$
		$\mathbf{D}^{\text{rand}}$	0.028	$(3.41, 0.954, 0.67)$	$(0.061, 0.14, 0.061)$

each estimate, for each set of pixels, the estimates are within 0.22 of the "true" parameter value. Though these estimates are close to the parameter value, many of the standard error estimates are still so small that the "true" parameter value is not covered by the 99% confidence interval. For each set of pixels, the 99% confidence interval of $\hat{v}_D$ does not cover the value $v_D = 1$.

We also considered damages defined through ellipses that have a vertical semi-axis which is larger than the horizontal semi-axis. In these examples, this inequality was not maintained in the parameter estimates which were computed using realizations of $\mathbf{D}_{ij}^{\text{rand}}$. In Table 6, we present the results for $(x_D, h_D, v_D) = (3, 0.5, 1)$. The estimates of $(\hat{x}_D, \hat{h}_D, \hat{v}_D)$ for the realization D_{ij} are farther from the "true" value than in the previous examples. This implies that the geometry of these ellipses poses a problem in the parameter estimation problem. This effect is amplified for the realizations $\mathrm{D}_{ij}^{\text{rand}}$. For the pixel sets "Left," "Even," and "All" the parameter estimation procedure produced an ellipse estimate with horizontal semi-axes longer than vertical semi-axes. Also, in these examples the estimate of the center $\hat{x}_D$ is larger than the value $x_D = 3$. The pixel set "Right" produced an estimate which was very close to the "true" value with each 95% confidence interval containing that "true" parameter value. The estimates using the realization of $\mathbf{D}_{ij}$ using the "Right" pixel set is the farthest from the true damage $(x_D, h_D, v_D) = (3, 0.5, 1)$ while the parameter estimate using the "Right" with realizations of $\mathbf{D}_{ij}^{\text{rand}}$ is the closest. This effect occurs because for data generated without pores, the "Right" pixels are the farthest from the damage centered at $x_D = 3$, so there is relatively little information in those pixel sets compared to the other pixel sets. For data generated using realizations of $\mathbf{D}_{ij}^{\text{rand}}$, the smaller the distance from the bottom of the damage to the source boundary (ω_4), the larger the error associated with $(u_D^{\text{rand}})_{ij}$ so the "Right" pixel set contains the least amount of error due to the approximation of $(u_D^{\text{rand}})_{ij}$ with U_{ij}. We see very similar results for the damage $(x_D, h_D, v_D) = (3, 0.5, 1.5)$ in Table 7.

When a damage with $v_D > h_D$ is placed in the horizontal center of the 10 by 2 rectangle, all of the pixel sets contain pixels directly below the center of the damage. Realizations of $\mathbf{D}_{ij}$ and $\mathbf{D}_{ij}^{\text{rand}}$ both yield relatively small standard errors compared to the difference between the parameter estimate and the true parameter set. It appears

Table 7: The estimated geometries for $(x_D, h_D, v_D) = (3, 0.5, 1.5)$

Nodes	$n \times m$	Data	$\hat{\sigma}^2$	$(\hat{x}_D, \hat{h}_D, \hat{v}_D)$	(SE($\hat{x}_D$),SE($\hat{h}_D$),SE($\hat{v}_D$))
Left	1012	$\mathbf{D}$	0.029	$(2.97, 0.5, 1.5)$	$(3.9 \times 10^{-3}, 6.8 \times 10^{-3}, 0.015)$
		$\mathbf{D}^{\text{rand}}$	0.043	$(3.14, 1.1, 0.9)$	$(0.039, 0.099, 0.057)$
Right	1012	$\mathbf{D}$	0.028	$(2.97, 0.469, 1.6)$	$(0.015, 0.012, 0.06)$
		$\mathbf{D}^{\text{rand}}$	0.037	$(2.59, 0.546, 1.8)$	$(0.051, 0.045, 0.22)$
Even	1012	$\mathbf{D}$	0.029	$(2.95, 0.5, 1.5)$	$(5.5 \times 10^{-3}, 8.3 \times 10^{-3}, 0.017)$
		$\mathbf{D}^{\text{rand}}$	0.04	$(3.19, 1.1, 0.91)$	$(0.06, 0.14, 0.069)$
All	1564	$\mathbf{D}$	0.025	$(2.97, 0.506, 1.5)$	$(3.6 \times 10^{-3}, 6.4 \times 10^{-3}, 0.015)$
		$\mathbf{D}^{\text{rand}}$	0.035	$(3.18, 1.14, 0.88)$	$(0.039, 0.1, 0.051)$

Table 8: The estimated geometries for $(x_D, h_D, v_D) = (5, 0.5, 1)$

Nodes	$n \times m$	Data	$\hat{\sigma}^2$	$(\hat{x}_D, \hat{h}_D, \hat{v}_D)$	(SE($\hat{x}_D$),SE($\hat{h}_D$),SE($\hat{v}_D$))
Left	1012	$\mathbf{D}$	0.029	$(4.98, 0.447, 1.1)$	$(0.021, 0.016, 0.036)$
		$\mathbf{D}^{\text{rand}}$	0.038	$(6.18, 0.633, 1.1)$	$(0.061, 0.061, 0.07)$
Right	1012	$\mathbf{D}$	0.028	$(4.98, 0.439, 1.1)$	$(0.023, 0.016, 0.039)$
		$\mathbf{D}^{\text{rand}}$	0.036	$(4.87, 0.729, 0.86)$	$(0.051, 0.065, 0.065)$
Even	1012	$\mathbf{D}$	0.029	$(4.99, 0.47, 1)$	$(0.031, 0.016, 0.051)$
		$\mathbf{D}^{\text{rand}}$	0.034	$(5.31, 1.2, 0.62)$	$(0.086, 0.21, 0.061)$
All	1564	$\mathbf{D}$	0.025	$(4.98, 0.483, 1)$	$(0.027, 0.012, 0.042)$
		$\mathbf{D}^{\text{rand}}$	0.027	$(5.29, 3.18, 0.41)$	$(0.13, 0.44, 0.016)$

Table 9: The estimated geometries for $(x_D, h_D, v_D) = (5, 0.5, 1.5)$

Nodes	$n \times m$	Data	$\hat{\sigma}^2$	$(\hat{x}_D, \hat{h}_D, \hat{v}_D)$	(SE($\hat{x}_D$),SE($\hat{h}_D$),SE($\hat{v}_D$))
Left	1012	$\mathbf{D}$	0.028	$(5.03, 0.482, 1.6)$	$(2.9 \times 10^{-3}, 6.4 \times 10^{-3}, 0.012)$
		$\mathbf{D}^{\text{rand}}$	0.054	$(5.92, 0.641, 1.7)$	$(0.014, 6.9 \times 10^{-3}, 0.039)$
Right	1012	$\mathbf{D}$	0.029	$(4.97, 0.487, 1.5)$	$(4.7 \times 10^{-3}, 6.4 \times 10^{-3}, 0.014)$
		$\mathbf{D}^{\text{rand}}$	0.053	$(4.75, 0.834, 1.2)$	$(0.035, 0.032, 0.047)$
Even	1012	$\mathbf{D}$	0.028	$(5, 0.491, 1.5)$	$(4 \times 10^{-3}, 7.3 \times 10^{-3}, 0.017)$
		$\mathbf{D}^{\text{rand}}$	0.045	$(5.15, 1.28, 0.84)$	$(0.071, 0.14, 0.053)$
All	1564	$\mathbf{D}$	0.025	$(5, 0.491, 1.5)$	$(3.2 \times 10^{-3}, 5.9 \times 10^{-3}, 0.013)$
		$\mathbf{D}^{\text{rand}}$	0.039	$(5.17, 1.42, 0.78)$	$(0.044, 0.12, 0.039)$

that in this case, the damage is not as well characterized. In Table 9, with $(x_D, h_D, v_D) = (5, 0.5, 1)$, the parameter estimates for the realization D_{ij} are closer to (5,0.5,1) than those of the realization $\mathrm{D}_{ij}^{\text{rand}}$. In many of these cases, the 95% confidence interval does not contain the true parameter value for this realization of $\mathbf{D}_{ij}$. Using the realization $\mathrm{D}_{ij}^{\text{rand}}$ in this example, the parameter estimates with pixel sets "Left" and "Right" maintain $\hat{v}_D > \hat{h}_D$ while parameter estimates with pixel sets "Even" and "All" invert this inequality resulting in the incorrect characterization $\hat{v}_D < \hat{h}_D$. The estimate of $\hat{x}_D = 6.18$ using the "Left" pixel set for the realization $\mathrm{D}_{ij}^{\text{rand}}$ is very far from $x_D = 5$ while the estimates of $\hat{x}_D$ for pixel sets "Right," "Even" and "All" are within 0.31 of $x_D = 5$. Though these estimates are different from the "true" parameter value, the standard errors are relatively small, resulting in the "true" parameter value being many standard errors from the parameter estimate. Again, for the larger damage $(x_D, h_D, v_D) = (5, 0.5, 1.5)$, we see similar results in Table 9.

In summary, our approximate homogenization model appears to work very well to *detect* damage while to *characterize* damage the homogenization approximation works well only in some cases but also is somewhat less satisfactory in other cases. This is dependent on shape of the damage (it appears to characterize damage with $h_D > v_D$ better than damage with $h_D < v_D$) and the choice of pixel set. One possible reason behind some of these inaccuracies in characterizing damage may be attributed to the large residuals obtained in many cases. We observe that large residuals produce larger values of the estimated variances $\hat{\sigma}^2$ (see (25), (26), and (28)) which in almost all table values are an order magnitude too large (recall $\sigma_0 = 0.015$ in all data D_{ij} and $\mathrm{D}_{ij}^{\text{rand}}$ generated). This leads to large SE and hence larger confidence intervals. This could, if these are given too much credence, lead to less than accurate assessments of one's ability to characterize the damage with these methods. Finally, for the given geometry investigated here using thermal probes, it is not surprising that characterization for damage with $v_D > h_D$ is not as accurate as that for examples with $h_D > v_D$. We note that the latter damages are expected to be more prevalent in composite materials of the type considered here where the damages tend to develop from enlarged "horizontal" pores resulting from the layered manufacturing process [3, 4, 5].

5 Conclusions

Based on previous results in [3, 4, 5], we considered using parameter estimation procedures in homogenized models to detect and characterize damage in porous materials. We found that these techniques could be used to *detect damage* very well for the considered damages in porous materials which were above 3% of the domain's area. In these examples, there was no clear difference between using data generated using the solution of the heat equation on a random perforated domain, and data generated using the homogenization approximation. On the other hand, in *characterization* of elliptical damage, there does appear to be a difference in using data generated using the solution of the heat equation on a perforated domain rather than using the homogenization approximation in estimating the center and the size of the elliptical damage. As one would expect, the estimates of the center and semi-axes lengths using data generated using the homogenization approximation were always closer to the true value than estimates of the center and semi-axes lengths using data generated using the solution of the heat equation on a perforated domain. The accuracy of the estimates of the center coordinate, horizontal semi-axis and the vertical semi-axis (x_D, h_D, v_D) varied over the examples using data generated the solution of the heat equation on the randomly perforated domain. The examples with $h_D < v_D$ did not preserve this inequality in the estimates of h_D and v_D in most cases while in the examples with $h_D > v_D$ the inequality was preserved. When we estimated (x_D, h_D, v_D) using data generated using the solution of the heat equation on the perforated domain, we observed significant differences between using different pixel sets. It appeared that some of the pixel sets were more sensitive to the error associated with using the homogenization approximation in the inverse problem. It is worthwhile to note that in most cases the estimated area of the damage was larger in the estimate than the area of the "true" damage. This suggests that this estimation procedure may not estimate the center nor the size correctly, often yielding an estimate that is larger. These methods could be used as a first estimate of damage which could be further resolved using a subsequent nondestructive evaluation technique.

Acknowledgements

This research was supported in part by the National Science Foundation under Research Training Grant (RTG) DMS-0636590 and in part by the Air Force Office of Scientific Research under grant number FA9550-09-1-0226.

References

[1] Charalambos D. Aliprantis and Owen Burkinshaw, *Principles of Real Analysis*, Elsevier North Holland, Inc., 1981.

[2] N. S. Bakhvalov and J Saint Jean Paulin, Homogenization for thermoconductivity in a porous medium with periods of different orders in the different directions, *Asymptotic Analysis*, **13** (1996), 253–276.

[3] H. T. Banks, Brittany Boudreaux, Amanda Keck Criner, Krista Foster, Cerena Uttal, Thomas Vogel, and William P. Winfree, Thermal based damage detection in porous materials, Technical Report CRSC-TR08-11, Center for Research in Scientific Computation, North Carolina State University, September, 2008; *Inverse Problems in Science and Engineering*, **18** (2010), 835–851.

[4] H T Banks, D. Cioranescu, A. K. Criner, and W P Winfree, Modeling the flash-heat experiment on porous domains, Technical Report CRSC-TR10-06, Center for Research in Scientific Computation, North Carolina State University, May, 2010; *Quarterly of Applied Mathematics*, S 0033-569X(2011)01230-8 (15pages)

[5] H. T. Banks, D. Cioranescu, A. K. Criner, and W P Winfree, Parameter estimation for the heat equation on perforated domains, Technical Report CRSC-TR11-06, Center for Research in Scientific Computation, North Carolina State University, April, 2011; *Journal of Inverse and Ill-Posed Problems*, DOI.10.1515/JIIP.2011.051 (33 pages).

[6] H. T. Banks, M. Davidian, J.R. Samuels Jr., and Karyn L. Sutton, An inverse problem statistical methodology summary, Technical Report CRSC-TR08-01, Center for Research in Scientific Computation, North Carolina State University, January, 2008; Chapter 11 in *Mathematical and Statistical Estimation Approaches in Epidemiology*, (edited by Gerardo Chowell, Mac Hyman, Luis M.A Bettencourt and Carlos Castillo-Chavez), Springer, Berlin Heidelberg New York, 2009, pp. 249–302.

[7] H. T. Banks, Sava Dediu, and S. L. Ernstberger, Sensitivity functions and their uses in inverse problems, *Journal of Inverse and Ill-Posed Problems*, **15** (2007), 683–708.

[8] H. T. Banks and B. G. Fitzpatrick, Statistical methods for model comparison in parameter estimation problems for distributed systems, *Journal of Mathematical Biology*, **28** (1990), 501–527.

[9] H.T Banks, K. Holm, and F. Kappel, Comparison of optimal design methods in inverse problems, Technical Report CRSC-TR10-11, Center for Research in Scientific Computation, North Carolina State University, July, 2010; *Inverse Problems*, **27** (2011), 075002.

[10] H. T. Banks and F. Kojima, Boundary shape identification problems in two dimensional domains related to thermal testing of materials, LCDS/CCS Rep. 88-6, April, 1988; *Quart. Applied Math.*, **47** (1989), 273–293.

[11] H. T. Banks, Fumio Kojima, and W. P. Winfree, Boundary estimation problems arising in thermal tomography, *Inverse Problems*, **6** (1990), 897–921.

[12] H.T. Banks and K. Kunisch, *Estimation Techniques for Distributed Parameter Systems*. Birkhausen, Bosten, 1989.

[13] H.T. Banks and H.T. Tran, *Mathematical and Experimental Modeling of Physical and Biological Processes*, CRC Press, Boca Raton, FL, 2009.

[14] Kathleen L. Bihari, *Analysis of Thermal Conductivity in Composite Adhesives*. PhD thesis, North Carolina State University, 2001.

[15] Horatio Scott Carslaw and John Conrad Jaeger, *Conduction of Heat in Solids*, Oxford University Press, 1959.

[16] D. Cioranescu, A. Damlamian, and G. Griso, The periodic unfolding method in homogenization, *SIAM Journal of Mathematical Analysis*, **40** (2008), 1585–1620.

[17] D. Cioranescu, A. Damlamian, and G. Griso, The periodic unfolding method in domains with holes, *to appear*, 2010.

[18] D. Cioranescu, P. Donato, and R. Zaki, Asymptotic behavior of elliptic problems in perforated domains with nonlinear boundary conditions, *Asymptotic Analysis*, **53** (2007), 209–235.

[19] D. Cioranescu and J Saint Jean Paulin, *Homogenization of Reticulated Structures*, Volume 136 of Applied Mathematical Sciences, Springer–Verlag, New York, 1999.

[20] Doina Cioranescu and Patrizia Donato, *An Introduction to Homogenization*, Oxford University Press, 1999.

[21] Doina Cioranescu, Patrizia Donato, and Rachad Zaki, The periodic unfolding method in perforated domains, *Portugaliae Mathematica*, **63** (2006), 467–496.

[22] Amanda Keck Criner, *Nondestructive Evaluation of Porous Materials*, Ph.D. Thesis, North Carolina State University, Raleigh, NC, August, 2011.

[23] M. Davidian and D.M. Giltinan, *Nonlinear models for repeated measurement data*, Chapman & Hall, 1995.

[24] P. Donato and A. Nabil, Homogenization and correctors for the heat equation in perforated domains, *Ricerche di Matematica*, **50** (2001), 115–144.

[25] W. J. Parker, R. J. Jenkings, C. P. Butler, and G. L. Abbott, Flash method of determining thermal diffusivity, heat capacity, and thermal conductivity, *Journal of Applied Physics*, **32** (1961), 1679–1684.

[26] Wenping Wang, Jiaye Wang, and Myung-Soo Kim, An algebraic condition for the separation of two ellipsoids, *Computer Aided Geometric Design*, **18** (2001), 531–539.